This is a repository copy of *Twin nucleation and variant selection in Mg alloys: An integrated crystal plasticity modelling and experimental approach*.

White Rose Research Online URL for this paper:
https://eprints.whiterose.ac.uk/171770/

Version: Accepted Version

Article:
Paramatmuni, C., Zheng, Z., Rainforth, W.M. orcid.org/0000-0003-3898-0318 et al. (1 more author) (2020) Twin nucleation and variant selection in Mg alloys: An integrated crystal plasticity modelling and experimental approach. International Journal of Plasticity, 135. 102778. ISSN 0749-6419

https://doi.org/10.1016/j.ijplas.2020.102778

Article available under the terms of the CC-BY-NC-ND licence (https://creativecommons.org/licenses/by-nc-nd/4.0/).

Reuse
This article is distributed under the terms of the Creative Commons Attribution-NonCommercial-NoDerivs (CC BY-NC-ND) licence. This licence only allows you to download this work and share it with others as long as you credit the authors, but you can't change the article in any way or use it commercially. More information and the full terms of the licence here: https://creativecommons.org/licenses/

Takedown
If you consider content in White Rose Research Online to be in breach of UK law, please notify us by emailing eprints@whiterose.ac.uk including the URL of the record and the reason for the withdrawal request.

eprints@whiterose.ac.uk
https://eprints.whiterose.ac.uk/

Twin nucleation and variant selection in Mg alloy: an integrated crystal plasticity modelling and experimental approach

Chaitanya Paramatmuni [a], Zebang Zheng [c], W. Mark Rainforth [b], Fionn PE Dunne [a]

a. Department of Materials, Imperial College London, London SW7 2AZ, United Kingdom
b. Department of Materials Science and Engineering, University of Sheffield, Sheffield S1 3JD, United Kingdom
c. School of Materials Science and Engineering, Northwestern Polytechnical University, China

Abstract

Extension twin nucleation and variant selection in magnesium alloy WE43 is investigated in experimentally characterised and deformed microstructures replicated in crystal plasticity models. Stored (dislocation) energy density is found to identify the experimentally observed locations of twins which are not otherwise explained by global Schmid factors or local resolved shear stress criteria. A critical stored energy of 0.015 Jm^{-2} was determined below which twin nucleation does not occur. The stored energy density explains the locations of the observed twins and the absence of twins in parent grains anticipated to be favourable for twin nucleation. Twin variant selection has been shown to be driven by minimising locally stored shear energy density, while the geometric compatibility and strain compatibility factors only aid in partial prediction. All experimentally observed variants were correctly determined.

Keywords: HCP; Twin nucleation; Rare-earth alloy; Stored energy density; Variant selection; Crystal plasticity.

1. Introduction

There is increasing interest in light metals in automobile industries and good strength to weight ratio makes Magnesium (Mg) alloy one of the candidate materials [Joost and Krajewski (2017)]. However, Magnesium and its alloys are limited by their poor formability and ductility due to the hexagonal close-packed (HCP) crystallographic anisotropy. Mg alloys commonly exhibit strong 'basal' texture with the basal poles aligned with the sheet normal direction after rolling [Styczynski et al. (2004), Mackenzie and Pekguleryuz (2008)]. Such texture results in modest work hardening and non-uniform elongation during deformation. It has been reported that the addition of rare earth (RE) elements, e.g. Cerium (Ce), Neodymium (Nd) and Yttrium (Y), can modify the conventional rolling texture [Bohlen et al. (2007), Hantzsche et al. (2010), Hadorn et al. (2013), Imandoust et al. (2017)]. Typical Mg-RE alloys exhibit a weak basal texture with the basal pole tilted towards the normal direction and transverse direction after rolling and/or annealing [Al-Samman and Li (2011), Guan et al. (2017a)]. The formability of Mg alloys can thus be improved by achieving a RE-texture which reduces the anisotropy.

At low temperatures, basal slip in Mg is activated at lower shear stress than prismatic or pyramidal systems, making $\langle a \rangle$-basal slip the preferred slip mode [Partridge (1967)]. Due to the limited number of easy slip systems in Mg alloys, deformation twinning that can accommodate strain along the crystal c-direction provides an alternative mode of plastic deformation. Twinning occurs by the formation of a nucleus which then propagates along the twin direction on the corresponding twin plane, where it continuously shears and reorients the parent grain [Christian and Mahajan (1995)]. It is therefore essential to understand the twinning mechanism to enable control over the microstructure and texture evolution.

The commonly observed twin mode in Mg alloys is the $\{10\bar{1}2\}[\bar{1}011]$ extension twin [Partridge (1967), El Kadiri et al. (2015)]. Due to the symmetry of the HCP crystal structure, there are six possible extension twin variants in Mg. Extensive work has been carried out to

establish the mechanistic basis of twin nucleation and variant selection. The most widely reported criterion is based on global Schmid factor that assumes a stress state resulting from remote loading conditions. Jonas et al. (2011) have shown that only half of activated twins have the highest global Schmid factors (e.g. >0.3). Similarly, statistical analysis of twin nucleation and corresponding microstructural features in Mg [Beyerlein et al. (2010)] and Zr [Capolungo et al. (2009)] show that 47%~60% of twins have the highest global Schmid factors on the activated variant, while the 21%~27% have the second highest. It is suggested that the local stress variation is responsible for the activation of twin variants with smaller global Schmid factors, although the local resolved shear stress has not been investigated quantitatively (see also [Livescu et al. (2019)]. In many modelling approaches, critical resolved shear stress (CRSS) is typically used to describe twin formation [Proust et al. (2009), Wang et al. (2013), Wu et al. (2015)]. A probabilistic twin nucleation model has been proposed by Beyerlein and Tomé (2010) which assumes a Poisson distribution of threshold shear stress to predict twin nucleation. This model was incorporated within crystal plasticity-phase field modelling [Liu et al. (2018)] to study the spatial twin formation process. However, experimental observations suggest that global Schmid factors calculated from macroscopic loading cannot fully explain the observed twins [Molodov et al. (2016), McClelland et al. (2015), Sevillano (2008), Livescu et al. (2019)]. This indicates that the twins are not always driven by stress alone. Gradients in plasticity established within parent grains can be mitigated by twin nucleation to achieve strain accommodation [McClelland et al. (2015)]. In the cases where twin nucleation is not stress driven, low/negative Schmid factors (non-Schmid) have been observed [Molodov et al. (2016)]. The negative Schmid factors may also result in negative local resolved shear stress associated with the observed active twin variant in the microstructure.

The non-Schmid twin variant selection is typically explained using the geometric compatibility factor and the shear strain accommodations. Both direct and indirect slip transmission may

50 occur at grain boundaries. Various models including the N factor [Livingston and Chalmers
51 (1957)], the geometric compatibility factor (m') [Luster and Morris (1995)], and the residual
52 burgers vector method (e.g. [Lim and Raj (1985)] have been utilised to investigate slip transfer.
53 Of these three factors, the geometric compatibility factor (m') has been extensively used as it
54 shows better predictions [Bieler et al. (2014), Guo et al. (2015)], and is based on the degree of
55 coplanarity of incoming and outgoing slip systems across the grain boundary. It was later
56 extended to investigate twin variant selection and twin-assisted-twinning in HCP materials
57 [Wang et al. (2010), Xin et al. (2015), Guo et al. (2014), Nervo et al. (2016), Kumar et al.
58 (2016)]. In addition, the selection of non-Schmid variants by the parent grain has also been
59 investigated by studying the shear strain accommodations that are required in the neighbouring
60 grain to permit twin variant formation [Jonas et al. (2011)]. It has been shown that the twin
61 variant which requires least strain accommodation by prismatic slip and the highest by basal
62 slip is selected by the parent grain.

63 Energy based criteria have also been employed to study twin formation. For instance, Wang
64 et al. (2012) proposed a deformation energy criterion for twin variant selection. The correct
65 prediction of variant selection increased from 50% using a global Schmid factor criterion to
66 80% using the energy criterion. The crystal plasticity finite element (CPFE) modelling work
67 by Cheng et al. [Cheng and Ghosh (2015), Cheng and Ghosh (2017)] also uses an energetic
68 criterion, where twin nucleation occurs when the initial energy of $\langle c + a \rangle$ dislocations
69 generated in the parent grain exceeds the energy of $\langle c + a \rangle$ dislocation dissociation event.
70 Similarly, the energetic twin nucleation model introduced by Capolungo and Beyerlein (2008)
71 is based on the dissociation of $\langle a \rangle$ type dislocations. From these studies it is evident that the
72 energy arising from slip to maintain the local dislocation structure may lead to twin nucleation.
73 In this context the local stored energy density, which is based on evolution of dislocation

structure, and which has been shown to be a driver for fatigue crack nucleation in materials [Wan et al. (2014), Chen et al. (2018)], may also be a useful approach.

Twin nucleation and variant selection are complex phenomena requiring knowledge of macroscopic loading, material properties, microstructure and the local stress and stored energy variations. In this paper, we utilise a systematic methodology which integrates a physically based crystal plasticity model and experiments aiming to establish new understanding of both twin nucleation and variant selection in WE43 alloy. In the next section, the experimental procedure and crystal plasticity approach are briefly outlined. Results are then presented, assessing twin nucleation and variant selection from the experimental observations, together with material property determination and comparison of the results with the CPFE analysis of twin nucleation. Finally, we investigate twin variant selection utilising both the experimental observations and CPFE calculations based on local stored energy. This is followed by discussion and conclusions.

2. Methodology

2.1 Experimental procedure

Mg alloy WE43 was received as an extruded bar supplied by Magnesium Elektron with the composition and texture shown in Guan et al. (2017b). Compression samples with dimensions of 4×4×8 mm (ASTM E9-09) were cut to calibrate the constitutive model and to investigate twin nucleation. The compression was performed along the transverse direction (TD) until ~5% strain in a Zwick/Roell™ 100 kN machine at room temperature at a strain rate of 0.1 s^{-1}.

Electron backscattered diffraction (EBSD) was performed on the sample before and after deformation in ZEISS Sigma 300™ SEM equipped with Bruker high resolution EBSD detector with voltage of 20 kV and ~13 mm working distance. The sample was mechanically polished until 4000 grit silicon carbide papers followed by fine polishing using 50 nm colloidal silica suspension for about 30 minutes. The sample was then Ar ion polished with a PECS-II system

under dual beam condition using 4.0 keV beam energy with rotational speed of 4 rpm for about 40 minutes, followed by 20 minutes fine polishing using 2.0 keV and a speed of 2 rpm. A large area of 831×505 μm^2 was scanned with step size of 3 µm to obtain the undeformed microstructure. After deformation, a sub-region of interest of area 159×122 μm^2 from this large area was further scanned for high resolution electron backscattered diffraction (HR-EBSD) analysis with a step size of 0.3 µm. The Kikuchi patterns with binning of 2×2 were saved for offline digital image cross-correlation.

2.2. Constitutive framework

The strain gradient and rate dependent crystal plasticity finite element formulation developed in Dunne et al. (2007) is utilized to study twin nucleation. A brief description of the formulation is presented here. The total deformation gradient $\mathbf{F}$ is decomposed into elastic ($\mathbf{F}^e$) and plastic deformation gradient tensors ($\mathbf{F}^p$) as

$$\mathbf{F} = \mathbf{F}^e\mathbf{F}^p \tag{1}$$

The plastic velocity gradient considers the contributions from all slip systems and is expressed as

$$\mathbf{L}^p = \sum_i \dot{\gamma}^i \mathbf{n}^i \otimes \mathbf{s}^i \tag{2}$$

where $\mathbf{n}^i$ and $\mathbf{s}^i$ are the plane normal and direction of slip system i respectively. The slip rate considering both forward and backward thermally activated dislocations escape is given by

$$\dot{\gamma}^i = \rho_m {b^i}^2 \nu_D \exp\left(-\frac{\Delta F}{kT}\right) \sinh\left(\frac{\left(\tau^i - \tau_c^i\right)\Delta V^i}{kT}\right) \tag{3}$$

in which ρ_m is the mobile dislocation density, b^i the Burgers vector magnitude, ν_D the Debye frequency, k the Boltzmann constant, T the temperature, τ^i and τ_c^i are the resolved shear stress

(RSS) and the corresponding critical resolved shear stress (CRSS) for slip system i. The strain rate sensitivity is determined by an activation energy ΔF and a corresponding activation volume ΔV^i for slip system i. The hardening law is given by the evolution of the CRSS based on the development of dislocation density as

$$\tau_c^i = \tau_{c0}^i + \alpha G b^i \sqrt{\rho_{SSD} + \sum_{i=1}^{n} \rho_{GND}^i} \tag{4}$$

where τ_{c0}^i is the initial slip resistance on the slip system, α the hardening coefficient and G the shear modulus. ρ_{SSD} and ρ_{GND} are the density of statistically stored (SSD) and geometrically necessary dislocations (GND) respectively. The SSD density is evolved as a function of plastic strain rate $\dot{p}$ at a material point as

$$\rho_{SSD} = \int_0^t \gamma' \dot{p}\, dt \tag{5}$$

where γ' determines the rate of density evolution. The distribution of GND density is calculated from strain gradients accommodating lattice curvatures. Further details of the GND calculation can be found in Dunne et al. (2012). In summary, the Nye tensor is related to the GND density on an individual slip system by

$$\text{curl}\left(\mathbf{F_p}\right) = \sum_{i=1}^{n} \mathbf{\Lambda^i} \rho_{gnd}^i \tag{1}$$

where $\mathbf{\Lambda^i}$ is the second order tensor that holds the slip system geometry information (details in Dunne et al. (2012)) and ρ_{GND}^i the GND density on slip system i.

The microstructure-sensitive stored energy density methodology presented by Wan et al. (2014), argued that 5% of energy due to plastic deformation is stored as dislocation structures and 95% is dissipated as heat. They derived the accumulated stored energy density G_{SE} at each microstructural point as

$$G_{SE} = \int \frac{\zeta |\boldsymbol{\sigma} : d\boldsymbol{\varepsilon}^{p}|}{\sqrt{\rho_{SSD} + \sum_{i=1}^{n} \rho_{GND}^{i}}} \tag{7}$$

in which ζ represents the fraction of plastic energy stored locally, i.e. $\zeta = 0.05$. The stored energy criterion has been extensively used to study crack nucleation and growth, and therefore to predict the fatigue life of materials [Chen et al. (2018), Wilson et al. (2019)]. In the present work, the accumulation of stored plastic energy in the material by the creation and evolution of dislocation structures is argued to be a key factor for twin nucleation. In the context of deformation twinning, the accumulation and dissociation of dislocations at the grain boundaries lead to the formation of twin nuclei [Jeong et al. (2018)]. Hence local stored energy density considered also by other authors [Capolungo and Beyerlein (2008), Cheng and Ghosh (2015), Cheng and Ghosh (2017)] is investigated, but here the particular form of energy in eqn. (7) is that stored by dislocation structure within an area determined by the dislocation density. The underpinning dislocation mechanistic basis is described in Zheng et al. (2019) and it is noted that the energy is stored predominantly by geometrically necessary dislocations.

3. Results

3.1 Deformed microstructure and experimental twin variant identification

Fig. 1(a) shows the microstructure before deformation with average grain size of 80 μm, where the highlighted dashed square indicates the section of microstructure considered for CPFE analysis and solid square indicates the region of interest (ROI) for HR-EBSD analysis. The deformed microstructure in the ROI (Fig. 1(b)), along with the HCP unit cells to indicate the grain orientations with respect to loading direction (TD), shows the presence of deformation twins with low area fractions. The primary observation is that twinning is not activated in the grain with most favourable crystallographic orientation for twinning (Grain P), but instead it is active in surrounding grains with least favourable crystallographic orientations. These grains

are henceforth referred to as grains A, B, C and D as shown in Fig. 1(b). In order to investigate twin nucleation, it is necessary to locate twin tips in these grains. Among grains A-D, the twin

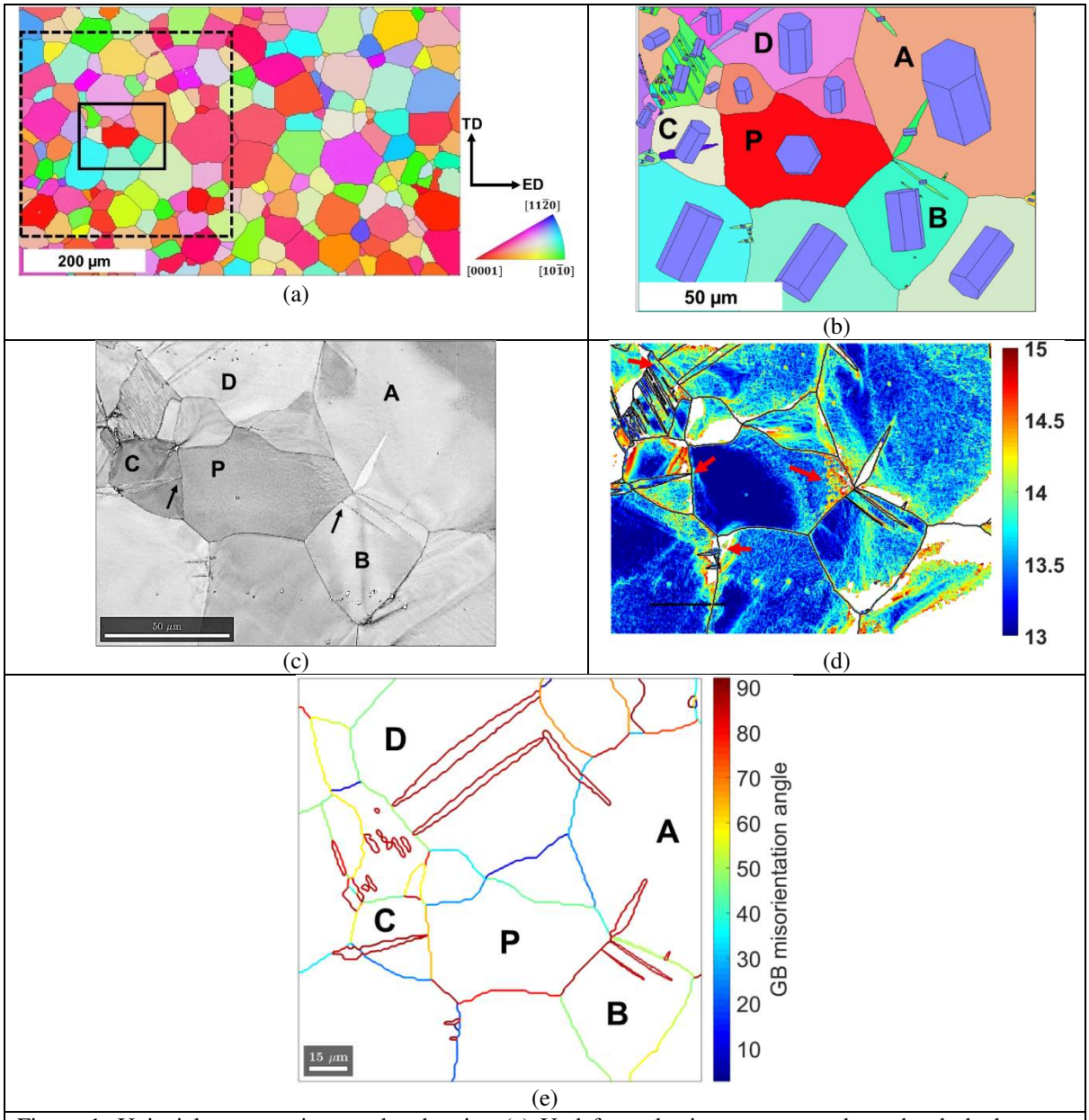

Figure 1: Uniaxial compression results showing (a) Undeformed microstructure, where the dashed square indicates the region of interest (ROI) for CPFE simulations and the solid line square indicates ROI for HR-EBSD analysis, (b) the ROI for HR-EBSD analysis after deformation with unit-cell orientations, (c) image quality map of the ROI and (d) GND density distribution in the ROI, where the red arrows show high GND density at twin tips (e) Grain boundaries (GB) of grains A-D and P showing misorientation angle

tips in grain C (right-hand tip) and B (left-hand tip) appear uncertain (see Fig. 1(b)). Therefore the image quality map (Fig. 1(c)) of the EBSD data is investigated, which confirms that the

tips of these twins in grain C and B are indeed at the respective parent grain boundaries (indicated using black arrows in Fig. 1(c)). Fig. 1(d) shows the distribution of GND density in the microstructure shown in Fig. 1(b). The GND distribution is heterogeneous within the grains and in particular at the vicinity of deformation twins, with high density at the twin tips (indicated using red arrows) compared to their respective twin boundaries. Fig. 1(d) also shows heterogenous distribution of GND density within the twin of grain C. It is shown in several studies that nucleation of twins at the high angle grain boundaries is typically assisted by local dislocations (slip-assisted), where the local high stress fluctuations drive twin nucleation and variant selection [Beyerlein et al. (2010), Beyerlein et al. (2011), Khosravani et al. (2015)]. Fig. 1(e) shows the grain boundary misorientation angles in the region of interest comprising grains A-D and P. One of the twins in grain A, which shares a boundary with grain D, appears to have nucleated at the grain boundary with a misorientation angle of ~35°. This misorientation angle and the presence of an adjoining twin in neighbouring grain D indicates that these twins may have nucleated through twin-assisted-twinning, which is consistent with independent studies [Khosravani et al. (2015)]. In contrast, the other twin in grain A that shares the boundary with grain B and P, appears to have nucleated close to the triple junction. Twins in grains B-D have nucleated at grain boundaries with higher misorientation angles (>40°), indicating that these are slip-assisted nucleation events.

There are six variants of extension twins (variants of $\{10\bar{1}2\}\langle 10\bar{1}1\rangle$) as shown in Table 1, therefore the next step is the identification of variant type of the twins in grains A-D. There are several methods to identify the twin variants such as by trace and orientation analysis [Jiang et al. (2008), Pei et al. (2012)]. In the current study the method of orientations is employed, where the crystallographic orientations of all six twin variants corresponding to parent grain orientation are calculated using the procedure outlined in [Niewczas (2010)]. Then the

Table 1: Extension twin variant types

Variant type	Crystallography
1	$(10\bar{1}2)[\bar{1}011]$
2	$(01\bar{1}2)[0\bar{1}11]$
3	$(\bar{1}102)[1\bar{1}01]$
4	$(\bar{1}012)[10\bar{1}1]$
5	$(0\bar{1}12)[01\bar{1}1]$
6	$(1\bar{1}02)[\bar{1}101]$

187

188 experimentally measured twin orientations are compared with these theoretical ones to identify
189 the active variants in the microstructure. Fig. 2 shows the basal pole figures consisting of
190 numerical and experimental twin orientations corresponding to grains A-D. Following the
191 procedure briefed earlier, the active variants are identified as variant 1 in grains A, B and D,

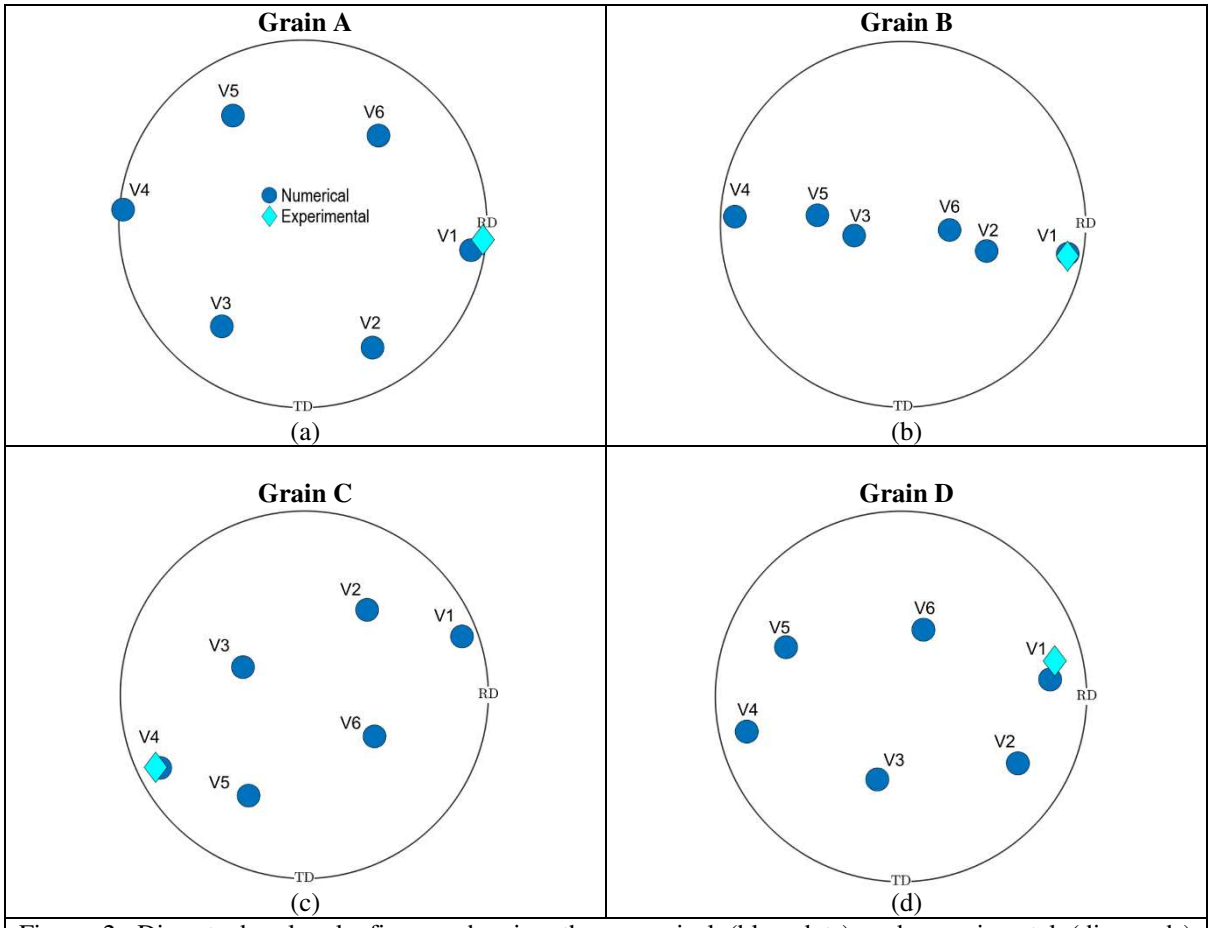

Figure 2: Discrete basal pole figures showing the numerical (blue dots) and experimental (diamonds) crystallographic orientations of twins in (a) Grain A, (b) Grain B, (c) Grain C and (d) Grain D. V# stands for variant (V) of type #.

192

193

while it is variant 4 in grain C. For the sake of completeness global Schmid factors, which rely on macroscopic loading direction, are also calculated to identify the type of twin variant active in the microstructure. Table 2 shows the Bunge Euler angles and global Schmid factors of all six variants of grains A-D, where the variants in bold are the active twin variants in the microstructure. From the table, except for grain C the global Schmid factors of active twin

Table 2: Global Schmid factors of twins, where bold indicates active twin variants

Grain ID	Euler angles			Global Schmid factors					
				Variant 1	Variant 2	Variant 3	Variant 4	Variant 5	Variant 6
A	194	36	171	**-0.15**	0.16	0.07	-0.16	0.09	0.02
B	187	86	171	**-0.48**	-0.47	-0.49	-0.49	-0.49	-0.49
C	150	161	193	0.17	0.37	-0.01	**0.20**	0.41	0.00
D	183	56	158	**-0.34**	-0.25	-0.16	-0.32	-0.29	-0.22

variants are all negative. Deformation twinning is a 3D unidirectional defect as opposed to slip. This implies that the global Schmid factors of active twin variants should always be positive. Therefore, the global Schmid factors fail to explain the nucleation and selection of twin variants in grains A, B and D. In the case of grain C non-Schmid twin variant selection is followed, where the variant corresponding to the third rank is selected. The other alternative explanation for the nucleation of these twins is the activation by fluctuations of local (favourable) stress states, which is now explored further.

3.2 Model material property determination

In order to determine the slip rule (eq. 3) properties for subsequent modelling, a three-dimensional polycrystalline CPFE model comprising 125 grains as shown in Fig. 3(a) was used. The grain morphologies were generated using 3D Voronoi tessellation software VGRAIN [Zhang et al. (2011)] with the average grain size of 80μm to be representative of the experimental microstructure, which are then discretised using C3D20R finite elements. The

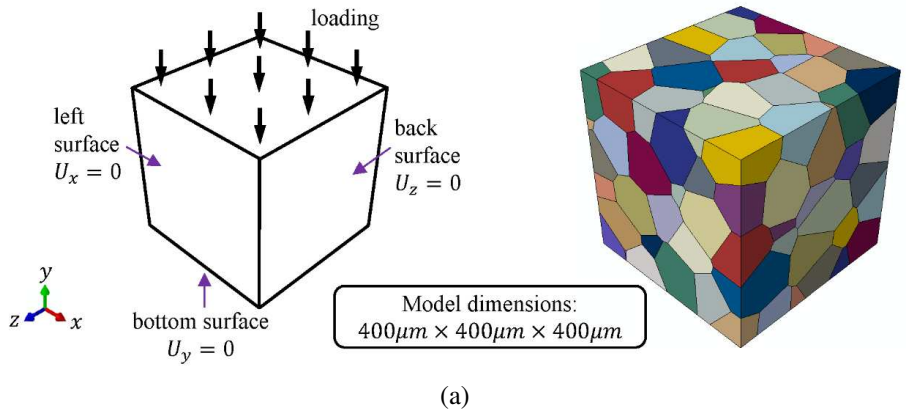

(a)

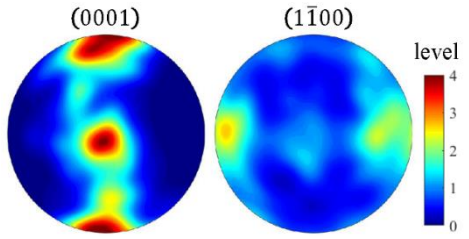

(b)

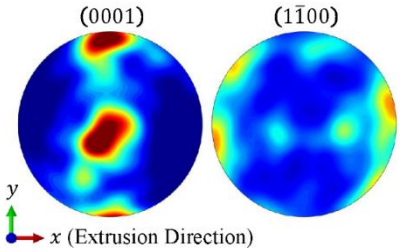

(c)

Figure 3: Polycrystal model set-up showing (a) The boundary conditions and polycrystal used for calibration, where the grain colours indicate grain IDs only (b) pole figure showing the orientations used for simulations and (c) the experimental pole figure.

crystal orientations were assigned from the EBSD map of the undeformed sample. The overall texture represented in the model and recorded from the experiment are shown in Fig. 3(b) and (c). Only 12 of the total 30 available slip systems $\{0001\} < 11\bar{2}0 >$, 3 prismatic slip systems $\{10\bar{1}0\} < 11\bar{2}0 >$, 6 pyramidal slip systems $\{\bar{1}\bar{1}22\} < 11\bar{2}3 >$ - are considered in the current study. The elastic stiffness tensor is defined as C_{11}=58.0, C_{12}=25.0, C_{13}=20.8, C_{33}=61.2, C_{44}=16.6 (GPa) [Tromans (2011)]. The material properties following the calibration process are listed in Table 3. The rate sensitivity parameters close to those experimentally measured by Bhattacharyya et al. (2016) are used in this study, where the activation volume of basal and prismatic slip is 100 b^3 and that of pyramidal slip is 6.25 b^3. The Debye frequency of Mg is calculated to be ~1.2×10^{13} s^{-1} [Kwak et al. (2016)].

Table 3: Single crystal parameters for WE43 at room temperature

Mode	τ_{c0} (MPa)	ΔV (b^3)	ΔF (J)	ρ_m (μm^{-2})	V_D (s^{-1})	γ' (μm^{-2})	α
Basal	14	100					
Prismatic	72.8	100	7.4×10^{-20}	1	1.2×10^{13}	1000	0.75
Pyramidal II order	126	6.25					

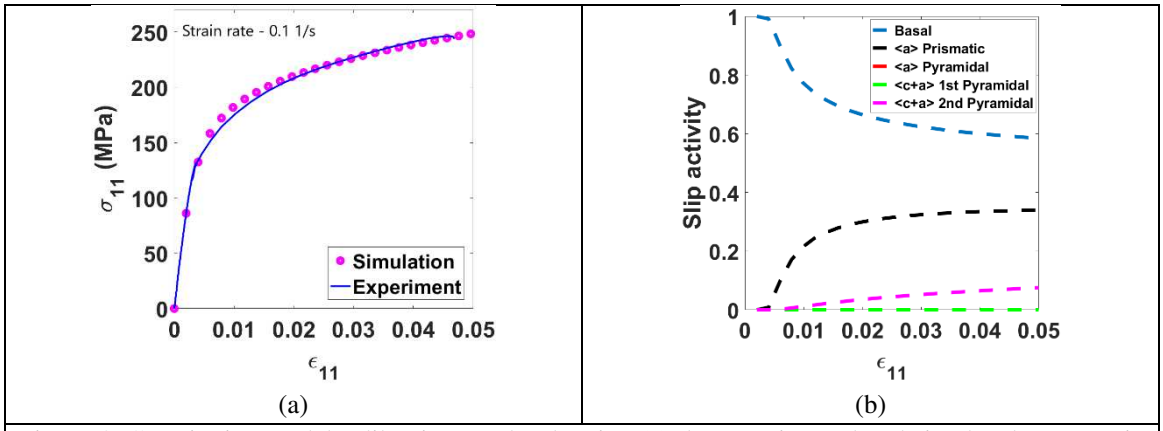

(a) (b)

Figure 4: Constitutive model calibration results showing (a) the experimental and simulated stress-stain curves and (b) the predicted slip activities

Fig. 4(a) shows the experimentally measured macroscopic true stress-strain response and the corresponding CPFE calculated response that shows good agreement with experiments. The slip activities during deformation are shown in Fig. 4(b). During compression, the basal slip system is activated first and is dominant at the onset of plastic deformation. Its activity decreases gradually with an increase in the contribution of other slip systems. Similar trends have been reported in independent studies (e.g. Bhattacharyya et al. (2016)).

3.3 Crystal plasticity analysis of twin nucleation

As discussed in section 3.1, global Schmid factors fail to explain the observed activation of twins. Therefore, the section of microstructure (Fig. 1(a)) including the grains of interest is explicitly replicated in the CPFE geometric model to study the local stress fields that may have

facilitated twin nucleation (prior to their incipient formation). Fig. 5(a) shows the microstructure and Fig. 5(b) the corresponding finite element mesh, which has an area of

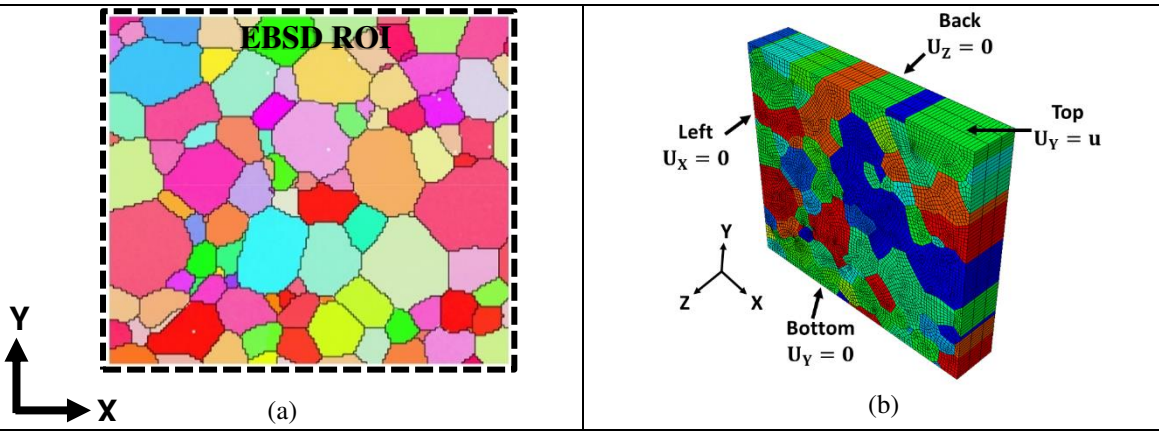

Figure 5: The simulation setup for twin nucleation studies showing (a) the region of interest and (b) the corresponding finite element mesh along with boundary conditions; the grain colours indicate one of the Bunge Euler angles (Φ).

446×397 μm^2 and thickness 80 μm. Note that we proactively replicate the experimental microstructure prior to the nucleation of twins, which are not, therefore, explicitly represented in the geometric model, since this establishes the stress states leading to twin nucleation. A limitation of the current approach is that the 2-D microstructure is extruded in the Z-direction to obtain a pseudo 3-D model, which does not contain sub-structure information. Many studies have shown that the sub-surface microstructure influences the spatial distribution of deformation fields [Zeghadi et al. (2007), Zhang et al. (2018)]. However, Zhang et al. (2018) have also shown that the presence of the sub-surface mostly only influences the magnitudes of GND density, relative lattice rotations and strain fields but does not alter the observed trends on the free surface. The model is loaded along direction Y (corresponding to TD) until 5% strain at the strain rate of 0.1 s^{-1}. Once this strain is reached, the model is unloaded.

Fig. 6(a) shows the calculated GND distribution within the grains of interest, where the CPFE geometric model is superimposed with the experimental grain boundaries to indicate twins and path XY indicates that along which GND density is measured. The distribution of GND density

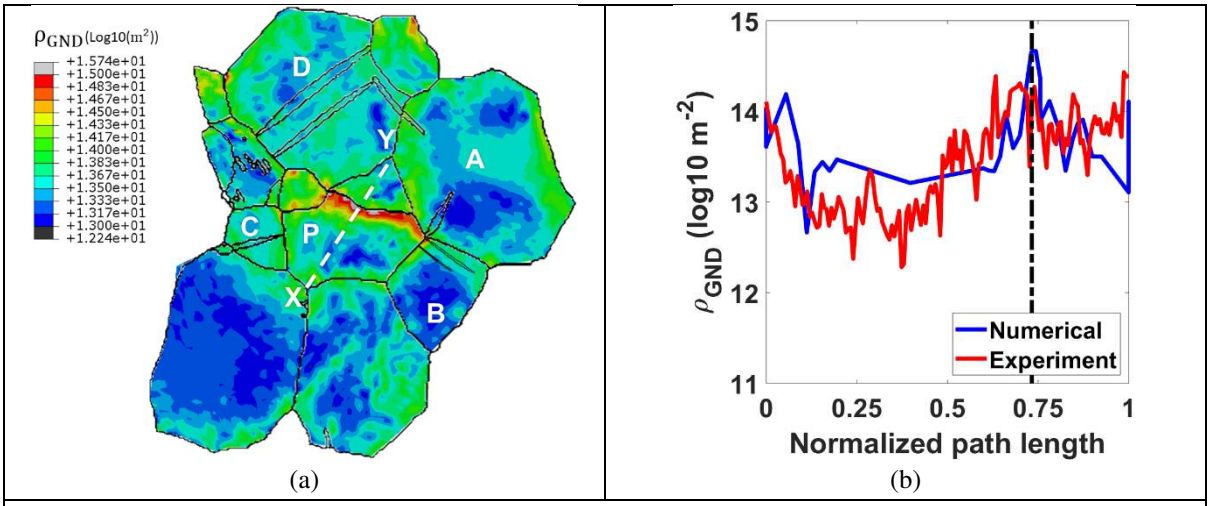

(a) (b)

Figure 6: The simulation results showing (a) the predicted GND density distribution in the grains of interest A-D, and (b) predicted and experimentally measured GND density along path XY. The grain boundary is shown with a black line.

along the path XY is shown in Fig. 6(b), in which the CPFE satisfactorily captures the experimental trends. Twin nucleation has in the literature been attributed to local stress states, where a twin nucleates when the (positive) RSS driven by local stress states reaches the CRSS of the particular twin type. Therefore, RSS is calculated here at the peak applied strain and examined for the active twin variants in grains A-D; that is, variants 1 and 4. Fig. 7(a) shows the spatial distribution of TRSS for variant 1, while Fig. 7(b) shows that for variant 4. The

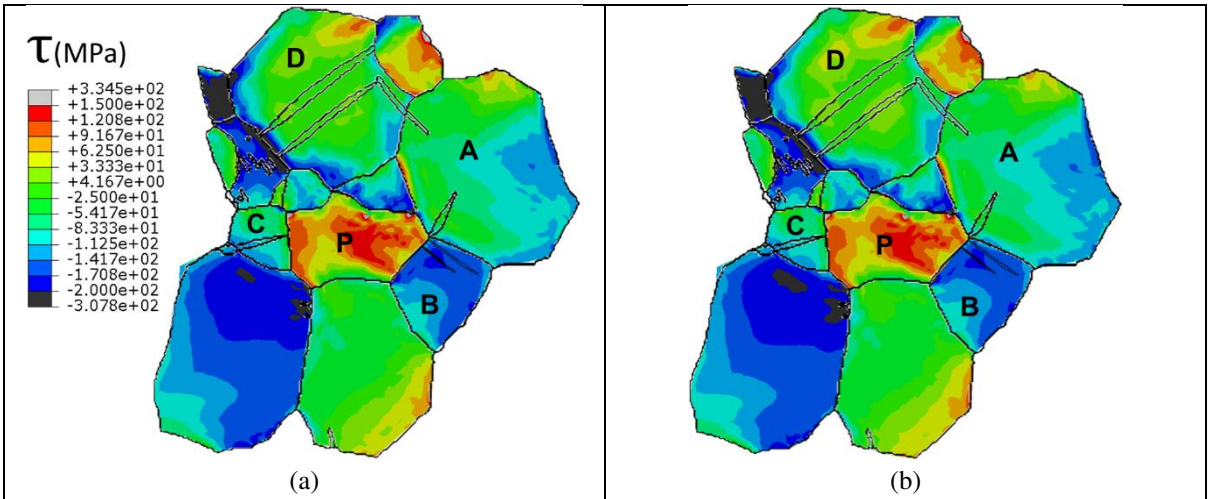

(a) (b)

Figure 7: The spatial distribution of twin resolved shear stress (τ) in grains A-D: (a) TRSS corresponding to variant 1 (b) TRSS corresponding to variant 4. Grain and twin boundaries are shown with black lines.

RSS in grain P is predominantly positive as expected considering the favourable crystallographic orientation, but this grain does not nucleate any twins. Another observation is that the RSSs corresponding to variant 1 (Fig. 7(a)) and variant 4 (Fig. 7(b)) are largely negative within grains A-D. This is also expected as the grain orientations (Table 2 and Fig. 1(b)) are least favourable. However, these are the grains within which twins are observed to nucleate, contrary to convention based on resolved shear stress for extension twins. This implies that the nucleation of these twins is not driven by local stresses that lead to high resolved shear stresses. Therefore, the concept of twin nucleation based on CRSS (stress driven) does not explain the activation of these twins in the microstructure. Nor does it explain the absence of twin formation in grain P.

Fig. 8 shows the spatial distribution of effective plastic strain and basal, prism and pyramidal slip respectively developed in grains A-D. The plastic strain and corresponding slip fields are heterogeneous with some relationship to the twin nucleation sites within the grains A, B and D. In particular, for grain A, one of the twins appears to nucleate from a location of high basal slip. For grain B, a high localised pyramidal slip and local basal slip is potentially related to twin nucleation, where the former is seen to make a considerable contribution to the effective plastic strain compared to other slip systems. Grain C shows a localised region of high basal slip on the right-hand boundary region close to where the narrow twin section is observed (suggesting nucleation end). For grain D, it's again basal slip which seems potentially to be related to both twins nucleating within this grain.

In summary, therefore, the hotspots in slip/plasticity are observed to have some relationship to observed twin nucleation occurrences in this microstructure, but it by no means precisely and unambiguously locates the twin nucleation sites in all cases. The study of local quantities within the microstructure from the CPFE compared with experimental observations therefore seem to suggest that while local GND density, resolved shear stress and accumulated slip are

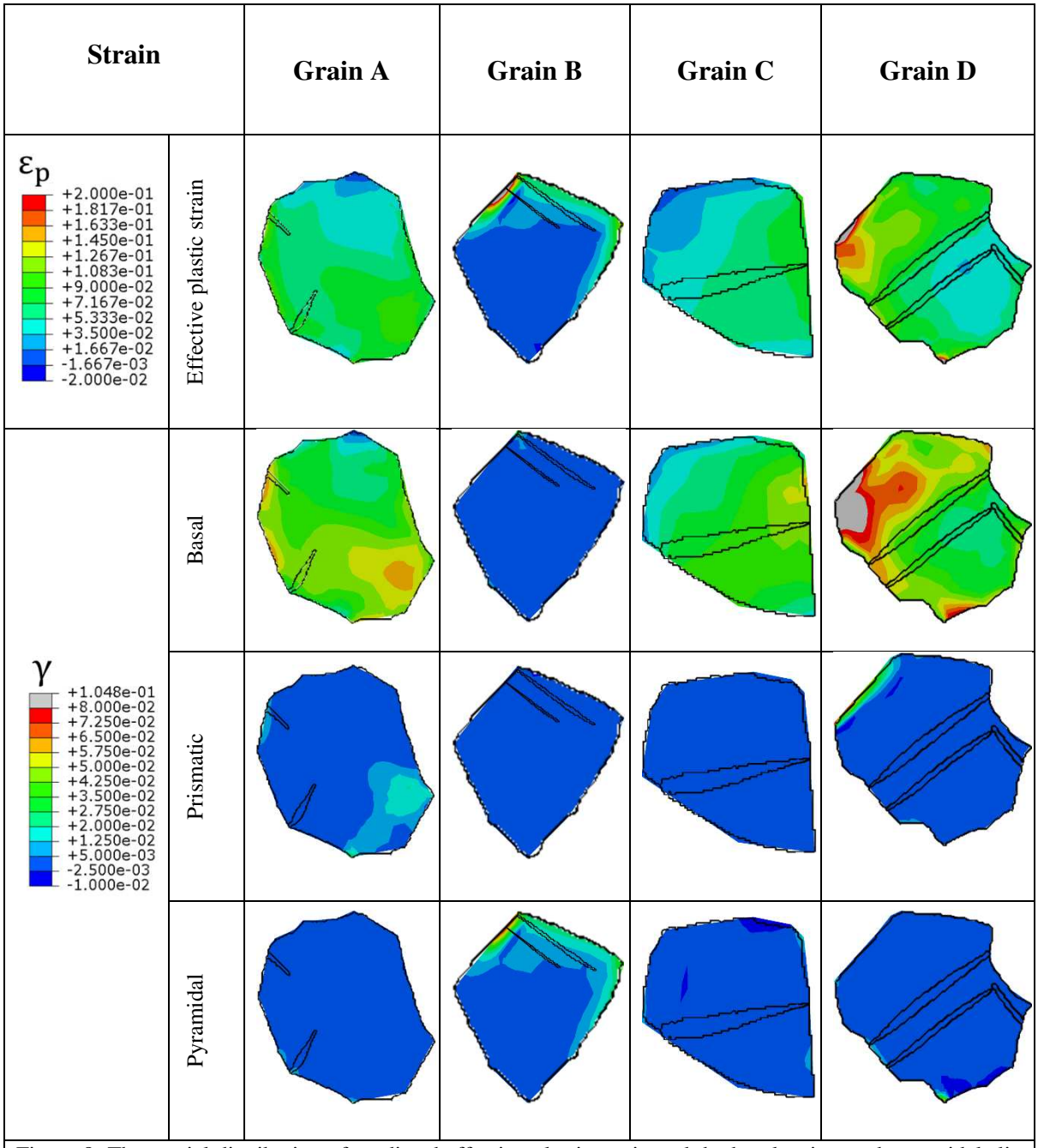

Figure 8: The spatial distribution of predicted effective plastic strain and the basal, prism and pyramidal slip fields in grains A-D as shown. Grain and twin boundaries are shown with black lines.

relevant and locally important to nucleating twins, they are not in their own right deterministic predictors of nucleation. We therefore turn to the energy approaches discussed in the introduction and in particular consider the dislocation-moderated stored energy density given in eqn. (7).

Fig. 9 (a)-(d) (i) shows the spatial distribution of stored energy density within grains A-D. Dashed lines indicate paths along which stored energy density is extracted for line-graph plots in (ii). Qualitatively, the stored energy density is observed to be consistently high within parent grains at the twin nucleation sites. For instance, observe the high stored energies within grains B and D in Fig. 9(b)(i) and Fig. 9(d)(i) at the vicinity of the twin nucleation sites.

Fig. 9 (a)-(d) (ii) shows the extracted stored energy densities measured along the paths shown (Fig. 9(i)) in grains A-D respectively, in which the black vertical lines indicate the experimentally observed twin nucleation sites. In grain A two twins are identified as AT1 and AT2, where the nucleation of AT1 appears to be slip assisted while AT2 (dashed line in Fig. 9 (a)(ii)) seems to be related to the secondary twin in grain D (see Fig. 7)). The focus, therefore, is on nucleation of AT1 but for the sake of completeness AT2 is also shown. From Fig. 9(a)(ii), the experimental nucleation site of AT1 corresponds to the highest stored energy along path P1-P2. Similarly for grain B in Fig. 9(b)(ii), the distinct peak in the stored energy corresponds to twin nucleation site BT2 in Fig. 9(b)(i) and twin BT1 nucleates close-by at a location also with high stored energy. While the latter is apparently not the highest energy density, the nucleation of BT2 is likely to perturb the distribution of energy density, and were the spatially resolved twin formation to be explicitly incorporated in the modelling, it is perfectly feasible that the subsequent highest energy location would shift (from BT2) to BT1. This phenomenon (redistribution of energy density) has been explicitly demonstrated in the context of secondary crack nucleation in other studies [Chen et al. (2017)]. In the case of grain C, the location of peak energy density corresponds exactly to the twin nucleation site. The stored energy, however, appears quite uniform along this particular grain boundary R1-R2 but again, once twin CT1 has been nucleated, the distribution of energy density and its magnitude is likely to be very different, and sufficiently dissipated to reduce the energy driver for additional twin nucleation anywhere else along this boundary.

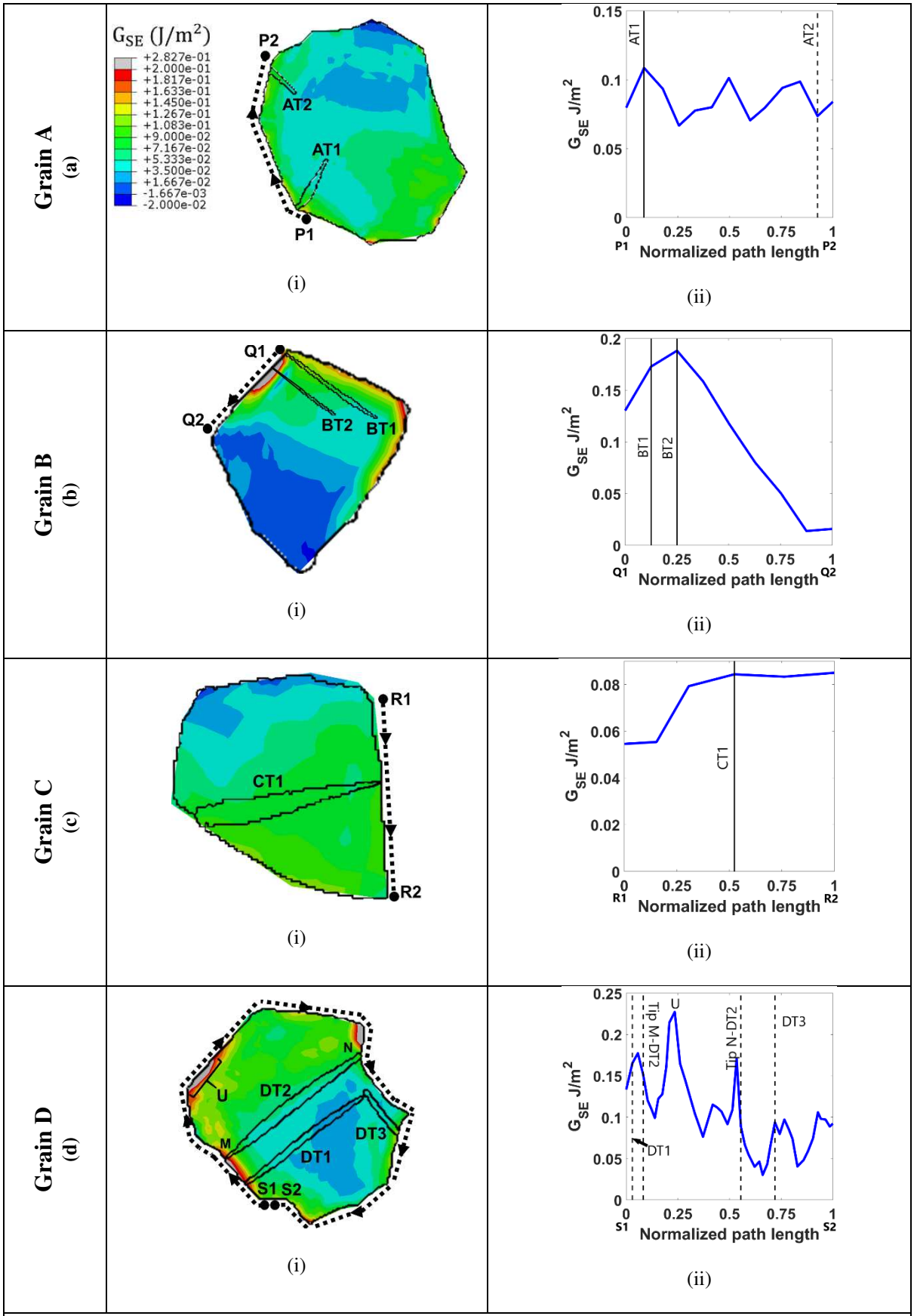

Figure 9: The calculated stored energy density (i) spatial distribution and (ii) along the paths (dashed lines) indicated in (i) for grains (a) A, (b) B, (c) C and (d) D. The solid black lines indicate the slip-assisted twin nucleation sites along respective paths.

Grain D nucleates three twins identified as DT1, DT2 and DT3. Twins DT1 and DT2 appear to have nucleated at the grain boundary by slip assisted nucleation, while DT3 seems to be secondary twin-assisted nucleation. The analysis in Fig. 9(d)(i) of the energy density at the left-most tip of DT1 shows high stored energy compared to the right-hand tip. Therefore, DT1 seems to have nucleated at the grain boundary. Twin DT2 also seems to originate from the high stored energy density location (M) common with DT1, but it is the case that a further region of high energy density is observed close to, but not at, the right-hand tip of twin DT2 (N). Fig. 9(d)(ii) shows the distribution of stored energy density measured along the path S1-S2 (Fig. 9(d)(i)). The energy density at the vicinity of location U (Fig. 9(d)(i)) is noted to be the highest along path S1-S2 and yet no twin is observed to nucleate at this location. In all the cases of slip-driven twin nucleation observed and analysed in this study, location U in grain D is the only example of a higher stored energy density being calculated in the absence of the observation of a twin nucleation. This observation, and the nucleation of twins DT1 and DT2 at energy densities lower than that in region U, is explicitly investigated later in section 3.4. All the results in Fig. 9 are shown for the peak applied strain (5%) such that any one value of peak stored energy density should not be inferred as a *critical* value to drive twin nucleation. Indeed, experimental observation suggests that in the alloy considered, twin nucleation initiates early in the loading history at about 100 MPa [Guan et al. (2019)], corresponding to an applied strain of about 0.002 (Fig. 4(a)). Hence, in order to extract out a definitive critical stored energy density required to cause twin nucleation, it is necessary to have knowledge of the calculated energy density at the point in the loading history when twin nucleation at a specific location is observed.

The peak energy densities extracted for grains A to D at applied peak strain of 5% (from Fig. 9 (ii)) are of order 0.11, 0.2, 0.08, and 0.175 Jm^{-2} respectively, such that a critical value must therefore be 0.08 Jm^{-2} (corresponding to grain C) or less. The full histories of the energy

densities at each of the key locations of twin nucleation can be extracted from the crystal plasticity analysis. On the basis that first twin nucleation was observed by Guan et al. (2019) at an applied stress of 100 MPa (corresponding to an applied strain of ~0.2%), it becomes possible to estimate the *critical* value of stored energy for twin nucleation using the model results for grain C, and the critical stored energy is estimated to be 0.015 Jm^{-2}. The absence of twins in grain P is notable, since this grain is apparently well-orientated and anticipated to nucleate twins. However, the accumulation of grain-averaged stored energy density with applied strain in grains A-D and P is shown in Fig. 10. From this figure, the accumulation is the least in grain P compared to grains A-D. Hence while twin nucleation criteria based on global Schmid factor and resolved shear stress would indicate grain P should twin, the stored energy density does not, in agreement with experimental observations. In addition, it is noted that grains A-C are immediate neighbours of grain P (Fig. 1(b)), wherein grains A and C nucleate twins much earlier in the deformation history. Hence it is argued that the nucleation of twins in grains A-D, as a consequence of higher accumulation of stored energy, relaxes and redistributes the energy such that grain P never attains the *critical* energy density.

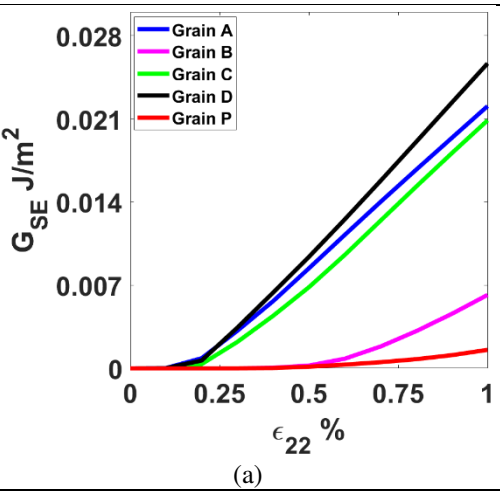

(a)

Figure 10: Accumulation of grain-averaged stored energy density shown until 1% strain in grains A-D and P

3.4 Twin variant selection analysis

The experimental observations in the current study indicate that neither the global Schmid factor nor the twin RSS analyses explain the twin nucleation and variant selection (Table 2 and Fig. 7) observations. Hence the geometric compatibility factor and shear strain accommodations are firstly explored to study the twin variant selection observations in grains A and B.

3.4.1 Geometric compatibility factor and shear strain accommodation analysis

Similar to slip transfer through interfaces, the geometric compatibility (m') between twin and slip can be defined as [Luster and Morris (1995)]

$$m' = \cos\varphi \times \cos\omega \tag{8}$$

where φ and ω are the angles between plane normal and shear direction of slip system in the neighbouring grain and twin systems in parent grain respectively. High m' means the slip system is well aligned with the twin variant and vice versa. The likelihood of strain transfer across the grain boundary by the nucleation of a twin in the parent grain increases as the value of m' approaches unity, while a low value (~0) of m' implies that the grain boundary is impenetrable. However, in the present experimental study the parent grain crystallographic orientations (A-D) are less favourable for twinning. Therefore, the value of m' is expected to be low compared to other independent studies.

The selection of non-Schmid twin variants by the parent grain has also been explained in the independent literature (e.g. [Jonas et al. (2011)]) on the basis of shear strain accommodation. In that work, the twin variant selected within the parent grain is expected to be that which requires least strain accommodation by prismatic slip and the highest by basal slip in the neighbouring grain. However, these studies were performed with grains that are favourably

384 oriented for twinning, which generate twins at lower strains and largely activate basal slip. In
385 the current study both the prismatic and basal slip collectively accommodate strain post-yield
386 (Fig. 4(b)). Therefore, the total ⟨a⟩ type shear is considered containing contributions from both
387 basal and prismatic slip. Thus, in this study, we firstly assess the criterion for variant selection
388 within the parent grain which is based on maximum ⟨a⟩ type shear accommodation in the
389 neighbouring grain in order to put the current work in the context of that in the open literature.
390 In addition, it transpires that the shear accommodation hypothesis and m' do not work. Hence
391 this is followed by the introduction of a new shear energy density criterion.

392 Following the procedure outlined in Jonas et al. (2011), the determination of accommodation
393 strains involve defining a displacement gradient tensor **S** in the twin reference frame, where
394 the X, Y and Z directions correspond to the shear direction, the shear plane normal, and the
395 cross product of X and Y directions respectively. All the components of **S** except the $\partial u/\partial z =$
396 s are zero, where s is the characteristic shear associated with a twin system (0.129 for extension
397 twins). The tensor **S** is given as

398 $$\mathbf{S} = \begin{pmatrix} 0 & 0 & s \\ 0 & 0 & 0 \\ 0 & 0 & 0 \end{pmatrix} \quad (9)$$

399 This displacement gradient tensor is then rotated onto the crystallographic reference frame of
400 the neighbouring grain to result in a new displacement gradient tensor e_{ij}, which contains all
401 nine non-zero components. The non-zero shear components are given a physical interpretation
402 in terms of the amount of shear strain required on a deformation mode in the neighbouring
403 grain to accommodate the formation of a twin variant in the parent grain [Jonas et al. (2011)].
404 Therefore, the main focus is on the shear components that correspond to shear on basal and
405 prismatic slip systems. In particular the shear on the basal slip is determined as $\left(|e_{xz}| + |e_{yz}|\right)$,
406 on prismatic slip is $\left(|e_{xy}| + |e_{yx}|\right)$ and finally the summation from shear on basal and prismatic
407 is the total ⟨a⟩ type shear.

Table 4 and 5 show the shear strains accommodation and m′ for all six possible twin variants for grains A and B respectively. The experimental results show that the twin variant 1 is selected by grain A (Fig. 2(a)). From Table 4, variants 1 and 6 have the maximum shear

Table 4. Shear accommodation and m′ analysis of Grain A (bold indicates the observed active variant)

Twin variants	Shear accommodation			m′	
	Basal	Prismatic	⟨a⟩ type	Basal	Prismatic
1	**0.14**	**0.07**	**0.21**	**0.41**	**0.28**
2	0.04	0.09	0.13	0.64	0.09
3	0.00	0.02	0.02	0.52	0.22
4	0.02	0.07	0.09	0.23	0.26
5	0.11	0.06	0.17	0.04	0.07
6	0.16	0.05	0.21	0.11	0.20

accommodation but among these two variants, the geometric compatibility factors for both basal and prismatic slip systems of variant 1 are greater than that of variant 6. Therefore, the preferred variant for grain A based on the two criteria is variant 1.

In grain B, the experimental active variant is also variant 1 (Fig. 2(b)). Among all the available six variants (Table 5), the 1st, 4th and 5th variants possess the same shear strain accommodation from the neighbouring grain, which means that these variants are equally probable.

Table 5. Shear accommodation and m′ analysis of Grain B (bold indicates the observed active variant)

Twin variants	Shear accommodation			m′	
	Basal	Prismatic	⟨a⟩ type	Basal	Prismatic
1	**0.08**	**0.11**	**0.19**	**0.21**	**0.49**
2	0.07	0.11	0.18	0.39	0.30
3	0.07	0.06	0.13	0.30	0.25
4	0.08	0.11	0.19	0.11	0.49
5	0.08	0.11	0.19	0.22	0.32
6	0.09	0.04	0.13	0.16	0.21

From the corresponding m' values, among variants 2, 4 and 5, variant 2 and 4 have the higher compatibility offered by prismatic slip, while variant 5 has the highest for basal slip and the least for prismatic slip. Therefore these two techniques lead to uncertainty in predicting the active variant in grain B.

In summary, the shear strain accommodation and m' factors have been considered to investigate the variant selection in parent grains A and B but transpiring only to be partially correct. The values of m' depend on the 'alignment' of slip systems in the neighbouring grains with the twin variant in the parent grain. The low values of m', as reported in the current investigation, have also been reported in independent studies [Wang et al. (2014), Liu et al. (2016), Zhou et al. (2020)], which emphasize the importance of investigating the effect of local deformation fields (stress, dislocation density etc.,) in twin variant selection. Zhou et al. (2020) have shown that, in slip assisted twinning, it is necessary to consider the local slip activity while predicting the twin variant selection using m'. Further, Wang et al. (2014) speculated that the nucleation of twins (in one of their grains of interest) within the grains with negative Schmid factor and low m' may occur due to high local stresses at the grain boundaries. Thus, we return to local stored energy density considerations to explain the experimental observations that may correctly identify the variant selection in all the cases.

3.4.2 Energy based investigation of variant selection

In an earlier section, stored energy density was shown to identify correctly the locations of experimentally observed twin nucleation sites, albeit with one location (region U) showing high energies in the absence of observed twins. Fig. 11(a) shows a schematic representation of one such location of high stored energy density (G_{SE}^{max}) in the parent grain along the grain boundary that serves as a high energy and defect source for a twin embryo formation. In order to assess variant selection, an appropriate energy density is also developed to account for the energy stored in the parent grain due to formation of a given twin variant. Experimental data

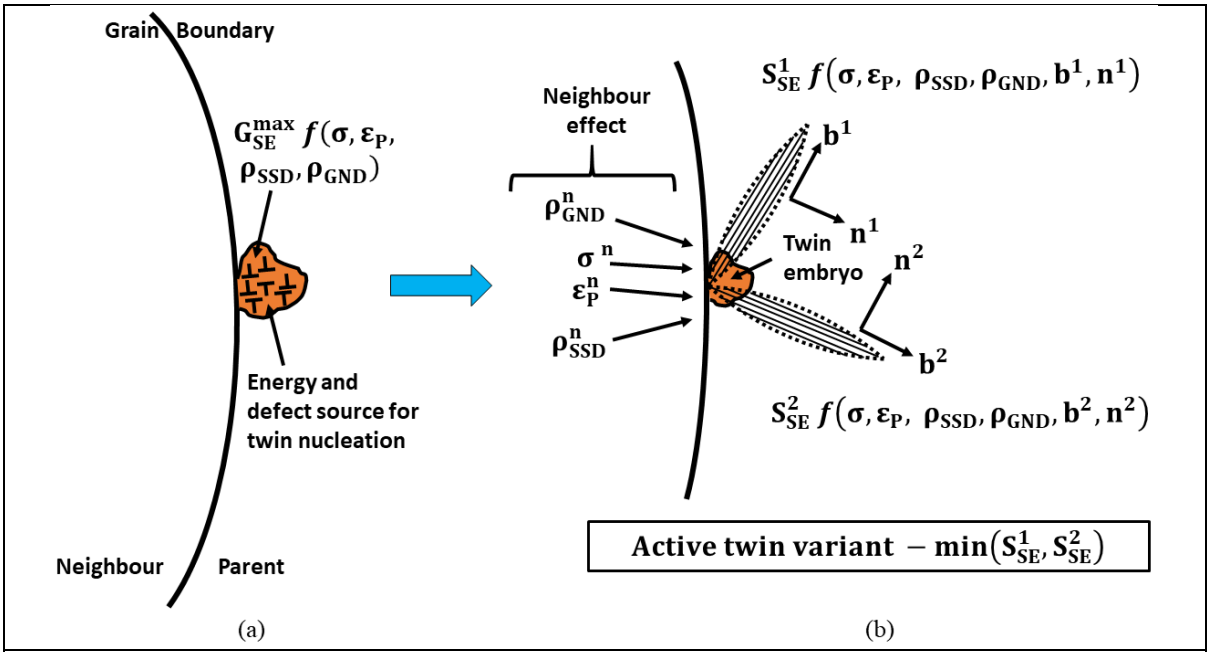

Figure 11: Schematic representation of twin nucleation and variant selection energy based criteria (a) location of high stored energy density (G_{SE}^{max}) along the grain boundary (b) twin variant selection criterion, operating at the location of G_{SE}^{max}, show only for 2 of 6 possible twin variants for the sake of clarity. S_{SE}^{1} and S_{SE}^{2} are the shear stored energy density of variants 1 and 2, and **b** and **n** are the twin shear direction and plane normal respectively.

reported in the literature show that the dislocation pile-up at the parent grain boundaries dissociate to form a twin nucleus, which further propagates and grows to form a twin. Therefore, the type of twin variant selected in the parent grain is decided at the incipient stage of nucleation at the parent grain boundaries. Beyerlein et al. (2011) have also observed a weak relationship between grain orientation and twin variant selection, and showed that the nucleation and variant selection are influenced strongly by the local high stress fluctuations at the grain boundaries. Hence an energy density term is established that is measured for all six twin variants at the parent grain boundaries to identify the twin variant.

It is shown in independent studies that a twin embryo forms by the dissociation of dislocations in the parent grain leading to formation of partials and twinning dislocations that shear the parent grain [Wang et al. (2009b)]. If φ^{β} is the total energy associated with the formation of an embryo of a twin variant β after the dissociation event, then this energy comprises that associated with the twin embryo (E_F^{β}) and work done (W_{ex}^{β}) by twinning dislocations

[Capolungo and Beyerlein (2008)]. This implies that the energy of the twin embryo (E_F^{β}) is stored in the material, while the work done is dissipated (lost). Therefore the total energy is given as [Nabarro (1952)]:

$$\varphi^{\beta} = E_F^{\beta} + W_{ex}^{\beta} \tag{10}$$

On a continuum scale, for a given stress state ($\boldsymbol{\sigma}$) and plastic strain state ($\boldsymbol{\varepsilon_P}$) at a given microstructural location in the parent grain, the total energy associated with formation of a given twin variant post dislocation dissociation event can be estimated as:

$$\varphi^{\beta} = (\boldsymbol{\sigma}: \mathbf{m^{\beta}})\ (\boldsymbol{\varepsilon_P}: \mathbf{m^{\beta}}) = \tau^{\beta}\, \gamma_P^{\beta} \tag{11}$$

where the plastic strain ($\boldsymbol{\varepsilon_P}$) is given as

$$\boldsymbol{\varepsilon_P} = \int_0^t \dot{\mathbf{d}}\boldsymbol{\varepsilon_P}\, dt \tag{12}$$

and $\mathbf{m^{\beta}}$ is the symmetric part of the Schmid tensor defined as $\mathbf{m^{\beta}} = \frac{\mathbf{1}}{\mathbf{2}}\Big(\big(\mathbf{b^{\beta}} \otimes \mathbf{n^{\beta}}\big) + \big(\mathbf{n^{\beta}} \otimes \mathbf{b^{\beta}}\big)\Big)$, where $\mathbf{n^{\beta}}$ and $\mathbf{b^{\beta}}$ are twinning plane normal and direction respectively, τ^{β} the resolved shear stress and γ_P^{β} the resolved accumulated shear strain of twin variant β. When dislocation pile up in a parent grain dissociates to form multiple twinning dislocations, they tend to form several variants of the same twin type [Mendelson (1969)]. Therefore it is necessary to determine the energies associated with all six twin variants to understand the variant selection.

It is shown in molecular dynamics studies that a stable twin embryo consists of either twinning dislocations only or twinning and partial dislocations [Wang et al. (2009a)] that extend to a thickness of several crystallographic planes [Wang et al. (2009b)]. Therefore in the present formulation, a 3D representation of twin embryo is assumed that has a volume of ΔV_T, with an

area of A_T and length L_T, where the length L_T is taken to be the local dislocation mean free distance λ. Thus the volume is given as

$$\Delta V_T = A_T L_T = \frac{A_T}{\sqrt{\rho_{SSD} + \sum_{i=1}^{n} \rho_{GND}^{i}}} \quad (13)$$

Then the shear energy density associated with the twin embryo that is stored in the system is given as

$$S_{SE} = \frac{E_F^{\beta}}{A_T} = \frac{\varphi^{\beta} \Delta V_T}{A_T} = \frac{\tau^{\beta} \gamma_P^{\beta}}{\sqrt{\rho_{SSD} + \sum_{i=1}^{n} \rho_{GND}^{i}}} \quad (14)$$

where the energy density associated with the twin embryo is called the shear stored energy, S_{SE} and equates to the stored twin embryo energy E_F^{β}. Further, for the formation of a stable twin embryo with an optimum distance between the twinning dislocations, the total energy associated with the formation of a twin variant (φ^{β}) should always be a minimum [Capolungo and Beyerlein (2008)], which implies that the energy of the twin embryo (E_F^{β}) should also be minimised for the chosen variant. Therefore in the current study, this energy S_{SE} ($= E_F^{\beta}/A_T$) is determined for all six twin variants at the parent grain boundaries where the total stored energy density is maximum in order to identify that twin variant which has minimum energy associated with its embryo formation. The schematic representation of one such twin embryo formation event is shown in Fig. 11(b), where for the sake of clarity only two of six twin variants are shown. At the location of peak G_{SE}^{max} location, it remains possible for any of the possible six twin variants to form. The particular twin variant selected is argued to be that which minimises the shear stored energy density (S_{SE}) for its formation compared with any other variant.

Fig. 12 shows the shear stored energy density calculated for all the twin variants in grains A-D, where this energy is measured along the same paths as the stored energy (Fig. 9(i)). For grain B, the shear strain accommodation and m' compatibility analysis was shown not to result in the correct observed variant selection, and that in fact twin variant 1 developed in this grain. Examining grain B first, therefore, Fig. 12(b) shows that at the twin nucleation sites BT1 and BT2 (black lines) where the stored energy density is high, twin variant one leads to the least

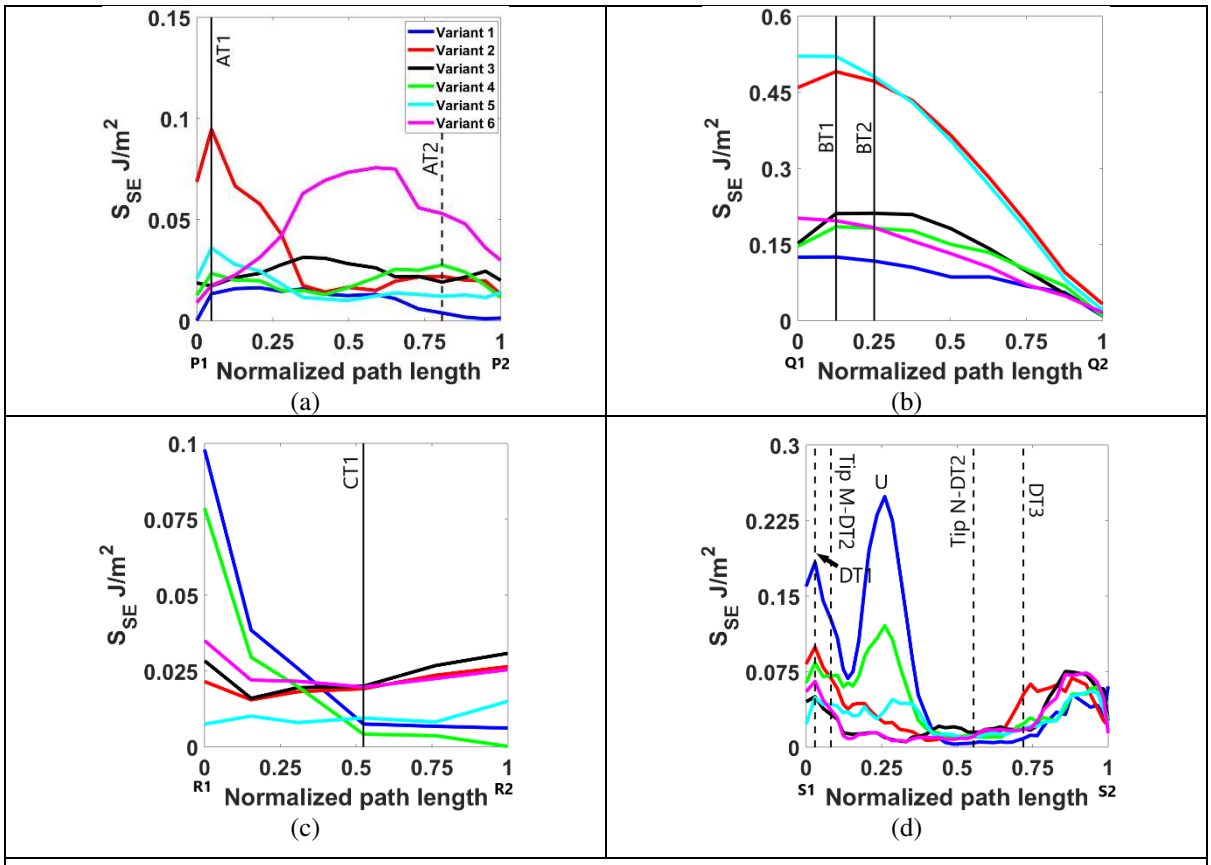

Figure 12: The shear stored energy quantified along the paths shown in Fig. 9(i) for grains (a) A, (b) B, (c) C and (d) D. The vertical lines indicate the experimentally observed twin nucleation sites, where the dashed lines indicate either the twin-assisted twin nucleation or ambiguous slip-assisted nucleation sites. The line colour indicates twin variant type shown in the legend.

shear stored energy compared to the other variants (and notably variant 4 and 5) and hence is selected by the parent grain. Similarly for grain A, both the twins AT1 (slip assisted) and AT2 (twin assisted) observed experimentally correspond to variant 1 and the predictions show least shear stored energy density for variant 1 at both the twin nucleation sites. This indicates that

520 the nucleation of twins assisted both by slip and twinning require least shear stored energy
521 density. Further, the shear stored energy criterion in this case is consistent with the shear strain
522 accommodation and m' analyses. For grain C, the shear stored energy correctly predicts the
523 experimentally observed active variant 4 in this grain. The distribution of stored energy density
524 in grain D led to ambiguity in predicting the twin nucleation site for twins DT1 and DT2 within
525 grain D (Fig. 9(d)(ii)). As mentioned earlier in the case of grain D, three twins DT1, DT2 and
526 DT3 of variant type 1 are experimentally observed. While the nucleation of DT3 is likely to be
527 twin-assisted, the nucleation of DT1 and DT2 are assisted by slip. DT1 has one of the twin tips
528 at the grain boundary and the other at the twin tip of DT3. From Fig. 9(d)(ii), high stored energy
529 indicates that DT1 may have nucleated at the grain boundary. However, Fig. 12(d) shows that
530 the shear stored energy for variant 1 at the grain boundary for DT1 is high. Therefore, it is
531 argued that the accumulation of high stored energy at the twin tip of DT3 due to its formation
532 may have nucleated DT1, which then propagated to the nearest grain boundary. It is shown in
533 independent studies that the formation of a twin results in high localization of stress [Kumar
534 et al. (2015)] and dislocation density [Guo et al. (2017)]. Similarly from Fig. 9(d)(ii), in the
535 case of DT2, high stored energy is observed at M and at the vicinity of N. However, the tip N
536 has the least shear stored energy for variant 1 compared to that of tip M. This implies that the
537 nucleation site of DT2 is indeed tip N instead of M (Fig. 12(d)). Further at tip N, the shear
538 stored energy of variant 1 is the least compared to the others. In addition the shear stored
539 energies for all the twin variant types at location U, which has the highest stored energy along
540 the path S1-S2 (Fig. 9(d)(i)), are high compared to those for both DT2 (tip N) and DT3. Hence
541 the absence of twin nucleation at region U for grain D results for two particular reasons. First,
542 the shear energy required for any twin variant in this region is very high compared with that at
543 observed twins DT2 and DT3. Second, the high stored energies and low shear energies
544 associated with twins DT2 and DT3 lead to early preferential nucleation of these twins, which

as a consequence dissipates energy, reducing the driving force for twin nucleation at region U. Therefore, this detailed analysis implies that the stored energy density in conjunction with the shear stored energy density appear to satisfactorily predict twin nucleation and variant selection. A grain boundary location giving rise to high stored energy and low shear stored energy is the most favourable for a twin nucleation site, where the twin variant selected is that requiring the least shear energy.

4. Discussion

In the current study extruded Mg alloy WE43 (Fig. 1(a)) is compressed until ~5% strain to nucleate extension twins with low/negative global Schmid factors. The CPFE calculations of the resolved shear stresses determined by the local stress states are negative for all twin variants (Fig. 7), which implies that these twins are not stress driven. The effective plastic strain shows hotspots in the microstructure, but this distribution does not precisely predict the twin nucleation sites. Therefore stored energy density, based on the evolution of local dislocation structures, has been used to investigate twin nucleation. Fig. 9 shows that the locations of high stored energy correspond to experimental twin nucleation sites in grains A-D. The stored energy approach of twin nucleation is similar to other independent studies based on heterogeneous twin nucleation theory [Capolungo and Beyerlein (2008), Beyerlein and Tomé (2010), Ghazisaeidi and Curtin (2013)], according to which a twin nucleates from the existing defects in the microstructure.

Independent experimental observations show that twins typically nucleate at low strain levels for which the formation of dislocation structures (and correspondingly stored energy) is likely to be limited, and for these cases, it is argued that the resolved shear stress (RSS) dominates the total stored energy (i.e. not the shear energy density determining variant selection) introduced above such that a simple RSS criterion is sufficient to explain twin nucleation (e.g. [Liu et al. (2017), Paramatmuni and Kanjarla (2019)]). However, in contrast, nucleation of

570 twins with negative Schmid factors at lower strains that are insensitive to grain orientations
571 have also been observed [Livescu et al. (2019)]. While variant selection was not addressed in
572 [Livescu et al. (2019)], it was suggested that the nucleation of such twins may have been caused
573 by fluctuations in local stress states. Similarly, independent experimental studies have reported
574 such microstructure insensitive twins may nucleate to maintain the compatibility, orientation
575 and strain gradients in the microstructure [McClelland et al. (2015), Molodov et al. (2016)]. In
576 the present study, which examines twins of just this kind, it has been shown that such twins are
577 not in fact nucleated by local stress states, but rather, by the stored energy density.

578 Variant selection was then investigated. It is shown that shear strain accommodation and the
579 geometric compatibility factor explain the observed variant selection in grain A only.
580 Therefore, a new shear energy-based criterion has been introduced, to study variant selection.
581 It is accepted that high stress concentration at the grain boundaries supply the energy required
582 for the formation of twins. Further, the grain boundaries act as sources of defects (partials or
583 twinning dislocations) required for formation of twin nucleus. The shear energy based criterion
584 introduced in this study is based on local stress variations and is sensitive to such local
585 dislocation structures, which act as defect sources for twin embryo formation. The observed
586 twin variants selected within grains A-D correspond to those that require least predicted shear
587 energy density of formation. It is interesting to note that the twins that are nucleated by a twin
588 in a neighbouring grain (twin-assisted-twinning) also show least shear stored energy (grains A
589 and D). This indicates that the energy of formation for a twin embryo is minimum although it
590 is driven by the high stress concentration and defects supplied by twins in neighbouring grain.
591 In summary, it is shown that the stored energy in conjunction with the shear stored energy
592 locates twin nucleation site and further determines the twin variant type (Fig. 11).

593 Other energy-based variant selection approaches have also been developed. For instance, Wang
594 et al. (2012) used an analytical plastic strain energy based approach to predict the active twin

variants in the microstructure, where the strain energy depends largely on the strain in the twin reference frame (ε_{33}^{twin}) and the mean free path of the twin ($\sqrt{L}$), given as $\left(\varepsilon_{33}^{twin}/\sqrt{L}\right)$. In their studies, the variant with highest absolute value of $\left(\varepsilon_{33}^{twin}/\sqrt{L}\right)$ was selected in the microstructure. Alternatively, if the sign of $\left(\varepsilon_{33}^{twin}/\sqrt{L}\right)$ is strictly considered, then the twin variant with the least value of $\left(\varepsilon_{33}^{twin}/\sqrt{L}\right)$ was chosen in their studies, which implies that the twin variant with the least associated plastic strain energy was selected in the microstructure. The shear stored energy approach is similar but more robust as it is based on the local stress fluctuations and dislocation structures. Further, an advantage is its implementation in full field approaches such as CPFE that includes the influence of neighbouring grains, evolving local dislocation structures and the strain field.

The stored energy density has been investigated to understand the absence of twins in the apparently most favourable grain P. Here, it was found that the rate of stored energy density accumulation was lowest for grain P, such that the critical energy required for twin nucleation was achieved earlier in other grains. The nucleation of twins in grains A-D in principle dissipate energy, redistribute stress, and correspondingly local stored energy such that the critical value required for twin nucleation does not develop in grain P. The *critical* stored energy for twin nucleation in this material is estimated to be 0.015 Jm^{-2}. The independent molecular dynamics and DFT studies have reported that the formation energy of twin boundaries decreases with increasing twin thickness, where a stable 9 layers thick twin embryo has a formation energy of ~0.256 J/m^{-2} (16 meV/A^{-2}) [Wang et al. (2009a)]. Assuming that this is the energy required for the formation of a twin embryo, the energy reported in the current study is about an order of magnitude less. This could be due to the length-scale and continuum approximation of the current CPFE approach. Further due to the weak texture, majority of the applied strain is

618 accommodated by crystallographic slip in this material. The accumulation of these dislocations
619 at the grain boundaries leads to stress concentration and act also as defect sources necessary
620 for twin embryo formation. Therefore the energy and source barriers for the formation of twins
621 is minimum, which is argued here to result in low *critical* stored energy for twin nucleation
622 compared to MD studies [Wang et al. (2009a)]. Further, while the MD studies (e.g. [Wang
623 et al. (2009a)]) provide complete localized understanding of twin formation, they do not
624 consider the effect of existing defects, alloying elements and suffers from the limitations of
625 computational cell size (not enough neighbouring grains). In addition, it appears that the MD
626 studies in [Wang et al. (2009a)] are within the bulk of pure Mg away from the grain boundary.
627 This is crucial as the high stress concentrations at the grain boundary may aid in overcoming
628 the energy barriers and reduce the total energy associated with the twin embryo, which in turn
629 reduces the energy of formation of twins.

630 **5. Conclusions**

631 - The experimental observations of compressed Mg alloy WE43 show the nucleation of
632 extension twins with low/negative global Schmid factors within unfavourable parent
633 grain orientations.

634 - The finite element based crystal plasticity analysis shows that the local resolved shear
635 stresses for these twins are negative implying that they are not driven by local stress.

636 - It is shown that the stored energy density offers mechanistic insight into twin nucleation
637 site, and acts as the driver of twin nucleation, indicating that these twins are driven
638 predominantly by local dislocation density.

639 - Based on the investigation of accumulated stored energy density calculated at the point
640 in the loading history when twins are first observed, a *critical* value of stored energy
641 for twin nucleation is estimated to be 0.015 Jm^{-2}.

642 - Twin variant selection is explained by the shear stored energy density, where the variant
643 selected is that which minimizes this energy density.

644 Therefore, the experimentally observed twin nucleation sites are identified by high stored
645 energy density (achieving the critical value first) and the variants selected by minimising the
646 stored shear energy which drives their formation.

647 **References**

648 [Al-Samman and Li (2011)] Al-Samman, T., Li, X., 2011. Sheet texture modification in
649 magnesium-based alloys by selective rare earth alloying. Materials Science and Engineering: A
650 528 (10-11), 3809–3822.

651 [Beyerlein et al. (2010)] Beyerlein, I., Capolungo, L., Marshall, P., McCabe, R., Tomé, C., 2010.
652 Statistical analyses of deformation twinning in magnesium. Philosophical Magazine 90 (16), 2161–
653 2190.

654 [Beyerlein et al. (2011)] Beyerlein, I., McCabe, R., Tomé, C., 2011. Effect of microstructure on the
655 nucleation of deformation twins in polycrystalline high-purity magnesium: A multi-scale modeling
656 study. Journal of the Mechanics and Physics of Solids 59 (5), 988 – 1003.

657 [Beyerlein and Tomé (2010)] Beyerlein, I., Tomé, C., 2010. A probabilistic twin nucleation model
658 for hcp polycrystalline metals. Proceedings of the Royal Society A: Mathematical, Physical and
659 Engineering Sciences 466 (2121), 2517–2544.

660 [Bhattacharyya et al. (2016)] Bhattacharyya, J., Wang, F., Wu, P., Whittington, W., El Kadiri, H.,
661 Agnew, S., 2016. Demonstration of alloying, thermal activation, and latent hardening effects on quasi-
662 static and dynamic polycrystal plasticity of mg alloy, we43-t5, plate. International Journal of Plasticity
663 81, 123–151.

664 [Bieler et al. (2014)] Bieler, T., Eisenlohr, P., Zhang, C., Phukan, H., Crimp, M., 2014. Grain
665 boundaries and interfaces in slip transfer. Current Opinion in Solid State and Materials Science 18 (4),
666 212–226.

667 [Bohlen et al. (2007)] Bohlen, J., Nürnberg, M. R., Senn, J. W., Letzig, D., Agnew, S. R., 2007. The
668 texture and anisotropy of magnesium–zinc–rare earth alloy sheets. Acta Materialia 55 (6), 2101–2112.

669 [Capolungo and Beyerlein (2008)] Capolungo, L., Beyerlein, I., 2008. Nucleation and stability of
670 twins in hcp metals. Physical review B 78 (2), 024117.

671 [Capolungo et al. (2009)] Capolungo, L., Marshall, P., McCabe, R., Beyerlein, I., Tomé, C.,
672 2009. Nucleation and growth of twins in zr: a statistical study. Acta Materialia 57 (20), 6047 – 6056.

673 [Chen et al. (2017)] Chen, B., Jiang, J., Dunne, F. P., 2017. Microstructurally-sensitive fatigue
674 crack nucleation in ni-based single and oligo crystals. Journal of the Mechanics and Physics of Solids
675 106, 15–33.

676 [Chen et al. (2018)] Chen, B., Jiang, J., Dunne, F. P., 2018. Is stored energy density the primary
677 meso-scale mechanistic driver for fatigue crack nucleation? International Journal of Plasticity 101, 213–
678 229.

679 [Cheng and Ghosh (2015)] Cheng, J., Ghosh, S., 2015. A crystal plasticity fe model for
680 deformation with twin nucleation in magnesium alloys. International Journal of Plasticity 67, 148–170.

681 [Cheng and Ghosh (2017)] Cheng, J., Ghosh, S., 2017. Crystal plasticity finite element modeling
682 of discrete twin evolution in polycrystalline magnesium. Journal of the Mechanics and Physics of Solids
683 99, 512–538.

684 [Christian and Mahajan (1995)] Christian, J. W., Mahajan, S., 1995. Deformation twinning. Progress
685 in materials science 39 (1-2), 1–157.

686 [Dunne et al. (2012)] Dunne, F., Kiwanuka, R., Wilkinson, A., 2012. Crystal plasticity analysis of
687 micro-deformation, lattice rotation and geometrically necessary dislocation density. In: Proc. R. Soc.
688 A. Vol. 468. The Royal Society, pp. 2509–2531.

689 [Dunne et al. (2007)] Dunne, F., Rugg, D., Walker, A., 2007. Lengthscale-dependent, elastically
690 anisotropic, physically-based hcp crystal plasticity: application to cold-dwell fatigue in ti alloys.
691 International Journal of Plasticity 23 (6), 1061–1083.

692 [El Kadiri et al. (2015)] El Kadiri, H., Barrett, C. D., Wang, J., Tomé, C. N., 2015. Why are {101 2}
693 twins profuse in magnesium? Acta Materialia 85, 354–361.

694 [Ghazisaeidi and Curtin (2013)] Ghazisaeidi, M., Curtin, W., 2013. Analysis of dissociation of< c>
695 and< c+ a> dislocations to nucleate twins in mg. Modelling and Simulation in Materials Science and
696 Engineering 21 (5), 055007.

697 [Guan et al. (2017a)] Guan, D., Rainforth, W. M., Gao, J., Sharp, J., Wynne, B., Ma, L., 2017.
698 Individual effect of recrystallisation nucleation sites on texture weakening in a magnesium alloy: Part
699 1-double twins. Acta Materialia 135, 14–24.

700 [Guan et al. (2017b)] Guan, D., Rainforth, W. M., Ma, L., Wynne, B., Gao, J., 2017. Twin
701 recrystallization mechanisms and exceptional contribution to texture evolution during annealing in a
702 magnesium alloy. Acta Materialia 126, 132–144.

[Guan et al. (2019)] Guan, D., Wynne, B., Gao, J., Huang, Y., Rainforth, W. M., 2019. Basal slip mediated tension twin variant selection in magnesium we43 alloy. Acta Materialia 170, 1–14.

[Guo et al. (2014)] Guo, C., Xin, R., Ding, C., Song, B., Liu, Q., 2014. Understanding of variant selection and twin patterns in compressed mg alloy sheets via combined analysis of schmid factor and strain compatibility factor. Materials Science and Engineering: A 609, 92–101.

[Guo et al. (2017)] Guo, Y., Abdolvand, H., Britton, T., Wilkinson, A., 2017. Growth of {} *twins in titanium*: *A combined experimental and modelling investigation of the local state of deformation*. *Acta Materialia* 126, 221–235.

[Guo et al. (2015)] Guo, Y., Collins, D., Tarleton, E., Hofmann, F., Tischler, J., Liu, W., Xu, R., Wilkinson, A., Britton, T., 2015. Measurements of stress fields near a grain boundary: Exploring blocked arrays of dislocations in 3d. Acta Materialia 96, 229–236.

[Hadorn et al. (2013)] Hadorn, J. P., Mulay, R. P., Hantzsche, K., Yi, S., Bohlen, J., Letzig, D., Agnew, S. R., 2013. Texture weakening effects in ce-containing mg alloys. Metallurgical and Materials Transactions A 44 (3), 1566–1576.

[Hantzsche et al. (2010)] Hantzsche, K., Bohlen, J., Wendt, J., Kainer, K., Yi, S., Letzig, D., 2010. Effect of rare earth additions on microstructure and texture development of magnesium alloy sheets. Scripta Materialia 63 (7), 725–730.

[Imandoust et al. (2017)] Imandoust, A., Barrett, C., Al-Samman, T., Inal, K., El Kadiri, H., 2017. A review on the effect of rare-earth elements on texture evolution during processing of magnesium alloys. Journal of materials science 52 (1), 1–29.

[Jeong et al. (2018)] Jeong, J., Alfreider, M., Konetschnik, R., Kiener, D., Oh, S. H., 2018. In-situ tem observation of {101 2} twin-dominated deformation of mg pillars: Twinning mechanism, size effects and rate dependency. Acta Materialia 158, 407–421.

[Jiang et al. (2008)] Jiang, J., Godfrey, A., Liu, W., Liu, Q., 2008. Identification and analysis of twinning variants during compression of a mg–al–zn alloy. Scripta Materialia 58 (2), 122–125.

[Jonas et al. (2011)] Jonas, J. J., Mu, S., Al-Samman, T., Gottstein, G., Jiang, L., Martin, E., 2011. The role of strain accommodation during the variant selection of primary twins in magnesium. Acta Materialia 59 (5), 2046–2056.

[Joost and Krajewski (2017)] Joost, W. J., Krajewski, P. E., 2017. Towards magnesium alloys for high-volume automotive applications. Scripta Materialia 128 (Supplement C), 107 – 112.

[Khosravani et al. (2015)] Khosravani, A., Fullwood, D., Adams, B., Rampton, T., Miles, M., Mishra, R., 2015. Nucleation and propagation of twins in az31 magnesium alloy. Acta Materialia 100, 202–214.

[Kumar et al. (2016)] Kumar, M. A., Beyerlein, I. J., McCabe, R. J., Tome, C. N., 2016. Grain neighbour effects on twin transmission in hexagonal close-packed materials. Nature communications 7.

[Kumar et al. (2015)] Kumar, M. A., Kanjarla, A., Niezgoda, S., Lebensohn, R., Tomé, C., 2015. Numerical study of the stress state of a deformation twin in magnesium. Acta Materialia 84, 349–358.

[Kwak et al. (2016)] Kwak, H., Xiao, J., Chaudhuri, S., 2016. Atoms-to-grains corrosion modeling for magnesium alloys. In: Essential Readings in Magnesium Technology. Springer, pp. 473–477.

[Lim and Raj (1985)] Lim, L., Raj, R., 1985. The role of residual dislocation arrays in slip induced cavitation, migration and dynamic recrystallization at grain boundaries. Acta Metallurgica 33 (12), 2205–2214.

[Liu et al. (2018)] Liu, C., Shanthraj, P., Diehl, M., Roters, F., Dong, S., Dong, J., Ding, W., Raabe, D., 2018. An integrated crystal plasticity–phase field model for spatially resolved twin nucleation, propagation, and growth in hexagonal materials. International Journal of Plasticity 106, 203–227.

[Liu et al. (2016)] Liu, G., Xin, R., Shu, X., Wang, C., Liu, Q., 2016. The mechanism of twinning activation and variant selection in magnesium alloys dominated by slip deformation. Journal of Alloys and Compounds 687, 352–359.

[Liu et al. (2017)] Liu, Y., Li, N., Kumar, M. A., Pathak, S., Wang, J., Mccabe, R. J., Mara, N. A., Tome, C. N., 2017. Experimentally quantifying critical stresses associated with basal slip and twinning in magnesium using micropillars. Acta Materialia 135, 411–421.

[Livescu et al. (2019)] Livescu, V., Beyerlein, I. J., Bronkhorst, C. A., Dippo, O. F., Ndefru, B. G., Capolungo, L., Mourad, H. M., 2019. Microstructure insensitive twinning: A statistical analysis of incipient twins in high-purity titanium. Materialia 6, 100303.

[Livingston and Chalmers (1957)] Livingston, J., Chalmers, B., 1957. Multiple slip in bicrystal deformation. Acta Metallurgica 5 (6), 322–327.

[Luster and Morris (1995)] Luster, J., Morris, M., 1995. Compatibility of deformation in two-phase ti-al alloys: Dependence on microstructure and orientation relationships. Metallurgical and Materials Transactions A 26 (7), 1745–1756.

[Mackenzie and Pekguleryuz (2008)] Mackenzie, L., Pekguleryuz, M., 2008. The recrystallization and texture of magnesium–zinc–cerium alloys. Scripta Materialia 59 (6), 665–668.

[McClelland et al. (2015)] McClelland, Z., Li, B., Horstemeyer, S., Brauer, S., Adedoyin, A., Hector Jr, L., Horstemeyer, M., 2015. Geometrically necessary twins in bending of a magnesium alloy. Materials Science and Engineering: A 645, 298–305.

[Mendelson (1969)] Mendelson, S., 1969. Zonal dislocations and twin lamellae in hcp metals. Materials Science and Engineering 4 (4), 231–242.

[Molodov et al. (2016)] Molodov, K. D., Al-Samman, T., Molodov, D. A., Gottstein, G., 2016. On the role of anomalous twinning in the plasticity of magnesium. Acta Materialia 103, 711–723.

[Nabarro (1952)] Nabarro, F. R. N., 1952. Mathematical theory of stationary dislocations. Advances in Physics 1 (3), 269–394.

[Nervo et al. (2016)] Nervo, L., King, A., Fitzner, A., Ludwig, W., Preuss, M., 2016. A study of deformation twinning in a titanium alloy by x-ray diffraction contrast tomography. Acta Materialia 105, 417–428.

[Niewczas (2010)] Niewczas, M., 2010. Lattice correspondence during twinning in hexagonal close-packed crystals. Acta Materialia 58 (17), 5848–5857.

[Paramatmuni and Kanjarla (2019)] Paramatmuni, C., Kanjarla, A. K., 2019. A crystal plasticity fft based study of deformation twinning, anisotropy and micromechanics in hcp materials: Application to az31 alloy. International Journal of Plasticity 113, 269 – 290.

[Partridge (1967)] Partridge, P. G., 1967. The crystallography and deformation modes of hexagonal close-packed metals. Metallurgical reviews 12 (1), 169–194.

[Pei et al. (2012)] Pei, Y., Godfrey, A., Jiang, J., Zhang, Y., Liu, W., Liu, Q., 2012. Extension twin variant selection during uniaxial compression of a magnesium alloy. Materials Science and Engineering: A 550, 138–145.

[Proust et al. (2009)] Proust, G., Tomé, C. N., Jain, A., Agnew, S. R., 2009. Modeling the effect of twinning and detwinning during strain-path changes of magnesium alloy az31. International Journal of Plasticity 25 (5), 861–880.

[Sevillano (2008)] Sevillano, J. G., 2008. Geometrically necessary twins and their associated size effects. Scripta Materialia 59 (2), 135–138.

[Styczynski et al. (2004)] Styczynski, A., Hartig, C., Bohlen, J., Letzig, D., 2004. Cold rolling textures in az31 wrought magnesium alloy. Scripta Materialia 50 (7), 943–947.

[Tromans (2011)] Tromans, D., 2011. Elastic anisotropy of hcp metal crystals and polycrystals. Int. J. Res. Rev. Appl. Sci 6 (4), 462–483.

[Wan et al. (2014)] Wan, V., MacLachlan, D., Dunne, F., 2014. A stored energy criterion for fatigue crack nucleation in polycrystals. International Journal of Fatigue 68, 90–102.

[Wang et al. (2014)] Wang, F., Sandlöbes, S., Diehl, M., Sharma, L., Roters, F., Raabe, D., 2014. In situ observation of collective grain-scale mechanics in mg and mg–rare earth alloys. Acta Materialia 80, 77–93.

[Wang et al. (2013)] Wang, H., Wu, P., Wang, J., Tomé, C., 2013. A crystal plasticity model for hexagonal close packed (hcp) crystals including twinning and de-twinning mechanisms. International Journal of Plasticity 49, 36–52.

[Wang et al. (2009a)] Wang, J., Hirth, J., Tomé, C., 2009. (1 012) twinning nucleation mechanisms in hexagonal-close-packed crystals. Acta Materialia 57 (18), 5521–5530.

[Wang et al. (2009b)] Wang, J., Hoagland, R., Hirth, J., Capolungo, L., Beyerlein, I., Tomé, C., 2009. Nucleation of a twin in hexagonal close-packed crystals. Scripta Materialia 61 (9), 903–906.

[Wang et al. (2010)] Wang, L., Eisenlohr, P., Yang, Y., Bieler, T., Crimp, M., 2010. Nucleation of paired twins at grain boundaries in titanium. Scripta Materialia 63 (8), 827–830.

[Wang et al. (2012)] Wang, S., Schuman, C., Bao, L., Lecomte, J., Zhang, Y., Raulot, J., Philippe, M., Zhao, X., Esling, C., 2012. Variant selection criterion for twin variants in titanium alloys deformed by rolling. Acta Materialia 60 (9), 3912–3919.

[Wilson et al. (2019)] Wilson, D., Wan, W., Dunne, F. P., 2019. Microstructurally-sensitive fatigue crack growth in hcp, bcc and fcc polycrystals. Journal of the Mechanics and Physics of Solids 126, 204–225.

[Wu et al. (2015)] Wu, P., Guo, X., Qiao, H., Lloyd, D., 2015. A constitutive model of twin nucleation, propagation and growth in magnesium crystals. Materials Science and Engineering: A 625, 140–145.

[Xin et al. (2015)] Xin, R., Liang, Y., Ding, C., Guo, C., Wang, B., Liu, Q., 2015. Geometrical compatibility factor analysis of paired extension twins in extruded mg–3al–1zn alloys. Materials & Design 86, 656–663.

[Zeghadi et al. (2007)] Zeghadi, A., Forest, S., Gourgues, A.-F., Bouaziz, O., 2007. Ensemble averaging stress–strain fields in polycrystalline aggregates with a constrained surface microstructure–part 2: Crystal plasticity. Philosophical Magazine 87 (8-9), 1425–1446.

826 [Zhang et al. (2011)] Zhang, P., Balint, D., Lin, J., 2011. Controlled poisson voronoi tessellation for
827 virtual grain structure generation: a statistical evaluation. Philosophical Magazine 91 (36), 4555–4573.

828 [Zhang et al. (2018)] Zhang, Z., Lunt, D., Abdolvand, H., Wilkinson, A. J., Preuss, M., Dunne, F. P.,
829 2018. Quantitative investigation of micro slip and localization in polycrystalline materials under
830 uniaxial tension. International Journal of Plasticity.

831 [Zheng et al. (2019)] Zheng, Z., Prastiti, N. G., Balint, D. S., Dunne, F. P., 2019. The dislocation
832 configurational energy density in discrete dislocation plasticity. Journal of the Mechanics and Physics
833 of Solids 129, 39–60.

834 [Zhou et al. (2020)] Zhou, B., Wang, L., Jin, P., Jia, H., Roven, H. J., Zeng, X., Li, Y., 2020.
835 Revealing slip-induced extension twinning behaviors dominated by micro deformation in a magnesium
836 alloy. International Journal of Plasticity, 102669.

837